

Ionization Balance in the Rotating Radiation Belt Accompanying Complete Divertor Detachment in LHD

Motoshi GOTO and Shigeru MORITA

National Institute for Fusion Science, Toki 509-5292, Japan

(Received 16 November 2007 / Accepted 15 February 2008)

A spectroscopic measurement is performed for a plasma in a rotating radiation belt, which accompanies the complete divertor detachment recently realized in the Large Helical Device (LHD) [J. Miyazawa *et al.*, Nucl. Fusion **46**, 532 (2006)]. The population distribution over the excited levels is experimentally determined from the Balmer series line intensities and is compared with the result of the collisional-radiative model calculation to determine the electron temperature T_e and density n_e . No reasonable pair of T_e and n_e is found when either the ionizing plasma or the recombining plasma is assumed. A good fitting is obtained under an assumption of the ionization balance plasma with $T_e = 1.8$ eV and $n_e = 2 \times 10^{20} \text{ m}^{-3}$. These parameters are confirmed through analysis of a high-wavelength-resolution measurement for the Balmer series lines which clearly exhibit the Stark broadening effect.

© 2008 The Japan Society of Plasma Science and Nuclear Fusion Research

Keywords: radiation belt, spectroscopy, ionization balance plasma, Stark broadening

DOI: 10.1585/pfr.3.S1042

1. Introduction

In the study of magnetically confined fusion plasma the reduction of heat flux on the divertor plate is an important issue. One of the solutions of this problem could be to induce plasma detachment in the divertor region through enhanced radiation loss. For this purpose, noble gas puffing has been attempted in various devices [1–5].

In the Large Helical Device (LHD), complete detachment of the divertor plasma has been obtained with strong puff of fuel gas (hydrogen) [6, 7]. A salient feature of the detached plasma is that it is accompanied by emergence of a luminous radiation belt in the boundary region. This radiation belt has a helical structure and appears to rotate poloidally with a frequency of, for example, 15 Hz.

Although the discharge conditions required to obtain such a detached plasma have been investigated in detail [7], the plasma state in the radiation belt itself is still unclear. Our interest is the plasma state in the strong radiation region and its relevance to the occurrence of plasma detachment. This paper describes our attempt to determine the plasma state and parameters, such as the electron temperature T_e and the electron density n_e , in the radiation belt from the spectra measured in the visible wavelength range.

2. Experiment

LHD is a heliotron-type, experimental fusion device with magnetic confinement. It forms steady-state helical magnetic fields using a set of super-conducting coils. The plasma has an elliptical poloidal cross-section, and it rotates with a toroidal pitch number of ten. The major and

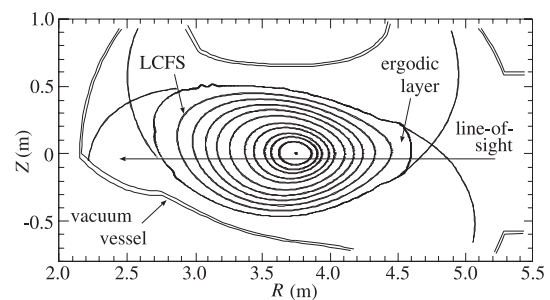


Fig. 1 Cross-sectional view of the elliptical plasma in LHD for the present study. The solid lines inside LCFS indicate the magnetic surfaces. The major radius of the vacuum vessel center is 3.9 m. The plasma is observed with a single line-of-sight shown with the arrow.

averaged minor radii of the last closed flux surface can be varied in the range of 3.5 m to 4.2 m and 0.3 m to 0.64 m, respectively.

We use an optical fiber with a diameter of 100 μm to observe the light in the visible wavelength region emitted from the plasma. One end of the optical fiber is placed at the observation port and its field of view is collimated with a lens ($f = 10$ mm). The diameter of the view area is roughly 30 mm at the plasma center. The optical axis passes through the plasma center as shown in Fig. 1. The other end of the optical fiber is located at the entrance of a UV-visible spectrometer. The spectrometer has a focal length of 50 cm and is equipped with three gratings of 100, 1800, and 3600 grooves/mm. The spectrum is recorded with a charge coupled device (CCD) detector. The CCD

author's e-mail: goto@nifs.ac.jp

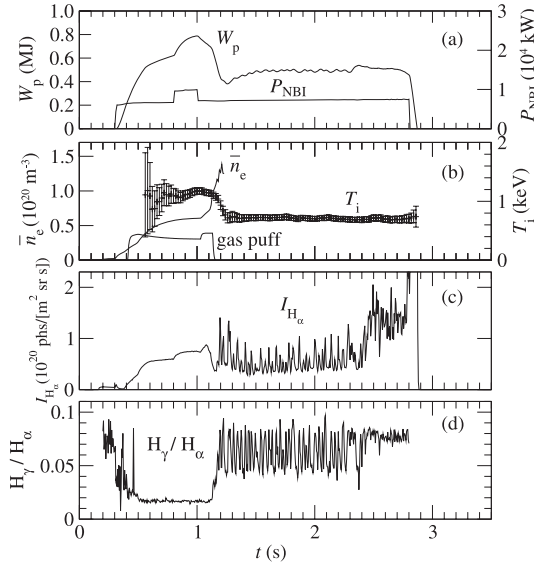


Fig. 2 Temporal development of the discharge for the present analysis: (a) stored energy W_p and NBI power P_{NBI} , (b) line-averaged electron density \bar{n}_e , ion temperature T_i , and gas puffing rate, (c) Balmer α line intensity, and (d) ratio of Balmer γ to Balmer α line intensities. \bar{n}_e measurement with the interferometer is unavailable after $t = 1.2$ s due to fringe jump. T_i measurement utilizes the Doppler width of a helium-like argon ion line.

consists of 1024 (in the direction of wavelength dispersion) times 256 (vertical to the former) pixels, and each pixel size is $26 \mu\text{m}$ square. In the present measurement, the electric charges accumulated in the CCD pixels are summed in the vertical direction and a single spectrum is obtained in each exposure sequence. The maximum acquisition frequency is $200 \text{ spectra s}^{-1}$. The sensitivity of the whole observation system has been absolutely calibrated with a tungsten lamp.

Figure 2 shows the temporal behavior of a discharge in which complete detachment is obtained. The present experiment employs the magnetic configuration of $R_{ax} = 3.65 \text{ m}$ and $B_{ax} = 2.712 \text{ T}$, where R_{ax} and B_{ax} are the magnetic axis position and the magnetic field strength on the magnetic axis, respectively. The plasma is sustained with three tangential neutral beams ($\sim 7 \text{ MW}$). The line-averaged electron density \bar{n}_e , which is measured with the interferometer, is feedback-controlled with the gas puffing rate until $t = 1 \text{ s}$. At $t = 1 \text{ s}$, a short-pulse massive gas puff ($\sim 0.1 \text{ s}$ and $\sim 200 \text{ Pa m}^3 \text{ s}^{-1}$) is supplied and \bar{n}_e increases suddenly. The \bar{n}_e measurement is unavailable after $t = 1.2 \text{ s}$ because of fringe jump.

After such an abrupt change in \bar{n}_e , the stored energy W_p and the central ion temperature T_i , which are measured with the diamagnetic coil and the Doppler broadening of the helium-like argon resonance line, respectively, are kept almost constant. During this stationary period, the particle flux on the divertor plate, which is measured with Langmuir probes, decreases considerably [6]. Simultaneous

measurement with an array of absolute extreme-ultraviolet photodiodes (AXUVD) [8] indicates the emergence of a rotating radiation belt [6].

Visible spectra of the light emitted from the plasma are measured with the 100-grooves/mm grating. The reciprocal linear dispersion is calibrated to be 19.957 nm/mm (0.51888 nm/pixel). The wavelength range of 300 to 700 nm can be simultaneously observed. Each emission line is fitted with a Gaussian function,

$$F_G(\lambda) = A \exp\left[-\left(\frac{\lambda - \lambda_0}{B}\right)^2\right] + C, \quad (1)$$

where λ_0 is the line center wavelength, and A , B , and C are the fitting parameters. The intensity I_G is then obtained as

$$I_G = AB \sqrt{\pi} \quad (\text{photons m}^{-2} \text{ sr}^{-1} \text{ s}^{-1}). \quad (2)$$

The temporal variations of the Balmer α (656.3 nm) line intensity and the intensity ratio of the Balmer γ (434.0 nm) to the Balmer α lines are shown in Fig. 2.

It is readily noticed that the Balmer α line intensity oscillates with a frequency of approximately 30 Hz, which is twice the frequency of the radiation belt rotation measured with the AXUVD measurement. This is understandable because the line intensity should take the maximum twice in every cycle of radiation belt rotation, when the radiation belt crosses the line-of-sight at the outboard-side and the inboard-side plasma edges. The ratio of the Balmer γ and Balmer α lines is also found to be oscillating with the same frequency. Since the change in the ratio of the Balmer γ to Balmer α line intensities is recognized to be a symptom of the switch between the ionizing plasma and the recombining plasma, this result suggests that the plasma states inside and outside the radiation belt are considerably different.

3. Collisional-Radiative Model

We use the collisional-radiative (CR) model code [9] for analyzing the obtained spectra. The CR model is based on the rate equations concerning the excited level populations. The time derivative of the population of a level p , $n(p)$, is expressed as

$$\frac{d}{dt}n(p) = \Gamma_{in}(p) - \Gamma_{out}(p), \quad (3)$$

where $\Gamma_{in}(p)$ and $\Gamma_{out}(p)$ denote population flows into the level p and those out of the level p , respectively. These population flows are explicitly written with the various elementary atomic processes as

$$\begin{aligned} \Gamma_{in}(p) &= \sum_{q>p} A(q, p)n(q) + \sum_{q<p} C(q, p)n_e n(q) \\ &\quad + \sum_{q>p} F(q, p)n_e n(q) + \beta(p)n_e n_i + \alpha(p)n_e^2 n_i \\ &= \sum_{q<p} C(q, p)n_e n(q) \\ &\quad + \sum_{q>p} \{F(q, p)n_e + A(q, p)\} n(q) \\ &\quad + \{\beta(p) + \alpha(p)n_e\} n_e n_i, \end{aligned} \quad (4)$$

and

$$\begin{aligned} \Gamma_{\text{out}}(p) &= S(p)n_e n(p) + \sum_{q>p} C(p, q)n_e n(p) \\ &\quad + \sum_{q<p} F(p, q)n_e n(p) + \sum_{q<p} A(p, q)n(p) \\ &= \left[S(p)n_e + \sum_{q>p} C(p, q)n_e \right. \\ &\quad \left. + \sum_{q<p} \{F(p, q)n_e + A(p, q)\} \right] n(p), \quad (5) \end{aligned}$$

respectively, where n_i is the ion density, $A(q, p)$ is the spontaneous transition probability, $S(p)$, $\alpha(p)$, and $\beta(p)$ are the rate coefficients for electron impact ionization, three-body recombination, and radiative recombination, respectively, and $C(p, q)$ and $F(p, q)$ are the excitation and deexcitation rate coefficients, respectively, due to electron impacts from level p to level q . The notation $\sum_{q>p}$ indicates that the summation is performed over the excited levels located higher than p .

The relaxation time of the excited level populations is generally so short that the left-hand-side of Eq. (3) is assumed to be zero excluding the ground state atom and the ion. In this case, a collection of Eq. (3) for all the excited levels is regarded as the coupled linear equations and expressed in matrix form as

$$\begin{pmatrix} \cdot & \cdot & \cdot & \cdot \\ \cdot & \cdot & \cdot & \cdot \\ \cdot & \cdot & \cdot & \cdot \\ \cdot & \cdot & \cdot & \cdot \end{pmatrix} \begin{pmatrix} n(2) \\ \cdot \\ n(p) \\ \cdot \end{pmatrix} = \begin{pmatrix} \cdot \\ \cdot \\ \cdot \\ \cdot \end{pmatrix} n_i + \begin{pmatrix} \cdot \\ \cdot \\ \cdot \\ \cdot \end{pmatrix} n(1), \quad (6)$$

where $n(1)$ is the ground state atom density. As the solution of these coupled linear equations, $n(p)$ is expressed as a linear combination of two terms, which are respectively proportional to n_i and $n(1)$ as

$$n(p) = R_0(p)n_e n_i + R_1(p)n_e n(1), \quad (7)$$

where $R_0(p)$ and $R_1(p)$ are the population coefficients and are functions of T_e and n_e . The first and second terms denote recombining and ionizing plasma components, respectively.

Equation (3) for $n(1)$ and n_i can be now rewritten in the form as

$$\frac{d}{dt}n(1) = -\frac{d}{dt}n_i = -S_{\text{CR}}n_e n(1) + \alpha_{\text{CR}}n_e n_i, \quad (8)$$

where S_{CR} and α_{CR} are defined as

$$S_{\text{CR}} = \sum_p S(p)n_e n(p), \quad (9)$$

$$\begin{aligned} \alpha_{\text{CR}} &= \{\beta(1) + \alpha(1)n_e\} n_e n_i \\ &\quad + \sum_p \{C(p, 1)n_e + A(p, 1)\} n(p), \quad (10) \end{aligned}$$

and correspond to the effective ionization and recombination rate coefficients, respectively. Their numerical values are found in Ref. [10].

4. Results

Figure 3 shows the spectrum when the Balmer α line intensity becomes maximum during the oscillation phase. This result is the average of the spectra picked up at the intensity maximums between $t = 1.2$ s and 2.2 s.

Each Balmer series line is fitted with a Gaussian function and the line intensity $I(p, q)$ [photons $\text{s}^{-1} \text{m}^{-2}$] is obtained. Here, p and q stand for the principal quantum number n of the upper and lower levels, respectively. From the viewpoint of atomic processes, the line intensity $I(p, q)$ is understood as

$$I(p, q) = N(p)A(p, q), \quad (11)$$

where $N(p)$ is the line-integrated population density of level p . We adopt $A(p, q)$ values of the NIST database [11] and derive $N(p)$ from Eq. (11). In Fig. 4 $N(p)$ normalized by their statistical weight $g(p)$ is plotted with the solid squares as a function of the ionization potential of level p . In the same figure, the population distributions in two other, different discharge phases are also shown. We attempt to fit all the population distributions in Fig. 4 with Eq. (7) by adjusting T_e and n_e .

The open triangles in Fig. 4 are taken in the time period from $t = 0.6$ s to 0.7 s. The population decreases rapidly with increasing principal quantum number. This behavior is a typical characteristic of the ionizing plasma, in which each level population is dominated by the second term in Eq. (7). Since the dependence of the population distribution on electron temperature and density is generally weak, it is difficult to uniquely determine those parameters from the obtained population distribution. The solid line is the calculation result with, for example, $T_e = 30$ eV and $n_e = 8 \times 10^{18} \text{m}^{-3}$ which is normalized to the measurement.

The open diamonds in Fig. 4 are the result at $t = 2.85$ s in the plasma decay phase after NBI heating is terminated. The result exhibits a typical characteristic of the recombining plasma; the populations of highly excited levels are relatively large. Roughly speaking, the slope of the highly

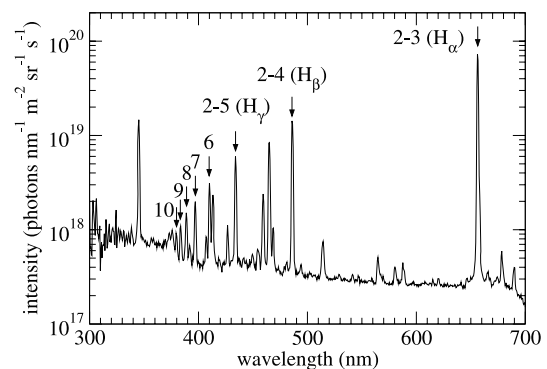


Fig. 3 Spectrum measured at the intensity maximum during the oscillation phase of the Balmer α intensity. The data are averaged between $t = 1.2$ s and 2.2 s.

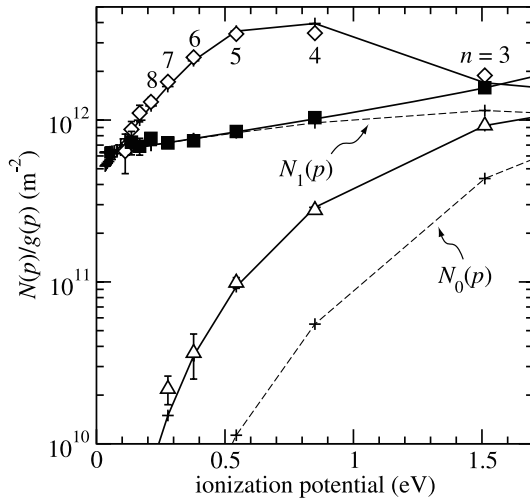


Fig. 4 Population distributions for three different plasma states; the solid squares, open triangles, and open diamonds are obtained for the intensity maximum during the oscillation phase of the Balmer α line intensity, before the detachment, and at the plasma terminating phase, respectively. Fitting results with the CR model are also shown with solid lines. The dashed lines labeled as $N_0(p)$ and $N_1(p)$ indicate the recombining and ionizing plasma components, respectively, in the total population $N(p)$ for the intensity maximum.

excited level populations corresponds to T_e and the maximum population level to n_e . We fit the result with the first term in Eq. (7), and the parameter values $T_e = 0.2$ eV and $n_e = 1.3 \times 10^{19} \text{ m}^{-3}$ are obtained. The fitting result is shown with a solid line in Fig. 4.

The solid squares in Fig. 4 show a distribution profile that is different from those in the former two cases. No reasonable combination of T_e and n_e is found for the present case when either the pure ionizing plasma or recombining plasma is assumed. Instead, we attempt fitting under the assumption of the ionization balance plasma. When the ionization rate and the recombination rate are balanced, i.e., when Eq. (8) is zero, the plasma is defined to be in ionization balance. The ratio of n_i to $n(1)$ is then expressed as

$$\frac{n_i}{n(1)} = \frac{\alpha_{\text{CR}}}{S_{\text{CR}}}, \quad (12)$$

and Eq. (7) is rewritten as

$$n(p) = \left\{ R_0(p) + R_1(p) \frac{S_{\text{CR}}}{\alpha_{\text{CR}}} \right\} n_e n_i. \quad (13)$$

The measured population distribution is well fitted with $T_e = 1.8$ eV and $n_e = 2 \times 10^{20} \text{ m}^{-3}$. The fitting result normalized to the measurement is shown with a solid line in Fig. 4. The dashed lines labeled as $N_0(p)$ and $N_1(p)$ correspond to the first and second terms in Eq. (7). Equation (13) is evaluated with these parameters and $n(3)/g(3) = 7.3 \times 10^{12} \text{ m}^{-3}$ is derived. The line-integrated population $N(3)/g(3)$ is, on the other hand, determined to be

$1.6 \times 10^{12} \text{ m}^{-2}$ in the measurement. The normalization factor between these quantities, $l = 0.22$ m, corresponds to the thickness of the radiation belt. This result is consistent with that of the AXUVD measurement.

The following should be noted regarding the intensity minimum in the oscillation phase. When the intensity takes a minimum, it is expected that the radiation belt is outside our field of view and the spectrum corresponding to the ionizing plasma is obtained. In reality, however, the observed spectrum is similar to that at the intensity maximum; i.e., the emission lines from highly excited levels are observed, but the Balmer α and β emissions are relatively strong. This result is interpreted as the superposition of the two radiation components: one from the boundary region of the bulk plasma and the other from the radiation belt that is reflected on the vacuum vessel wall. Only Balmer α and β lines in the Balmer series lines might be dominated by the radiation from the boundary region and their intensities are relatively strong.

5. Discussion

In the present analysis, T_e is mainly determined from $n(p)$ over highly excited levels ($p \geq 6$). However, the wavelength resolution in the measured spectrum is insufficient and the number of lines discretely observed are limited up to $p = 2$ -11. In addition, the intensity of lines from the levels higher than $p = 9$ have large uncertainty. With a measurement at higher wavelength resolution, the lines from levels higher than $p = 11$ could be resolved and the uncertainty in the line intensity be reduced. Such improvements should increase the reliability of T_e derived in the previous section. Furthermore, since n_e is rather high, lines from highly excited levels should exhibit Stark broadening. If the broadening is observable with the higher resolution measurement, n_e can be evaluated independently and the value obtained in the previous section can be cross-checked.

Here, we focus our interest on the measurement with high-wavelength resolution of the lines from the levels higher than $p = 7$. The same spectrometer is used but the grating is replaced with one having 1800 grooves/mm. The reciprocal linear dispersion with the present grating is 1.0843 nm/mm ($2.8191 \times 10^{-2} \text{ nm/pixel}$). The observed spectrum is shown in Fig. 5. The intensity is normalized to the synthetic spectrum which is discussed later. The Balmer series lines of $n = 2$ -7 to $n = 2$ -13 are observed clearly. The line width increases as the upper level of the transition moves upward. This result suggests the Stark broadening effect.

We attempt to synthesize the spectrum in the wavelength range in Fig. 5 with the parameters derived in the previous section and compare it with the measurement result. Each discrete line is characterized by its intensity and shape. The intensity can be expressed as $n(p)A(p, q)$ as mentioned above. We assume the local thermodynamic

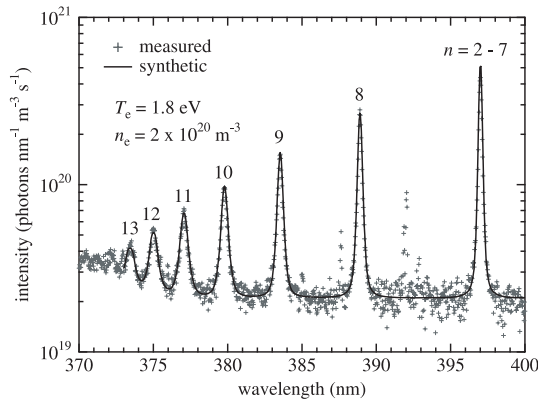


Fig. 5 Spectrum measured at the intensity maximum with a high-wavelength-resolution measurement (crosses). Balmer series lines corresponding to $n = 2-7$ to $n = 2-13$ transitions are observed discretely. The solid line is a synthetic spectrum calculated under the LTE condition with $T_e = 1.8$ eV and $n_e = 2 \times 10^{20} \text{ m}^{-3}$. Stark broadening, Doppler broadening, and the instrumental function are taken into account for each line shape.

equilibrium (LTE) condition for $n(p)$ distribution over the corresponding excited levels. Under LTE, $n(p)$ is expressed with the Saha-Boltzmann equation as

$$n(p) = p^2 \left(\frac{h^2}{2\pi m k T_e} \right)^{3/2} \exp\left(\frac{R}{p^2 k T_e} \right) n_e n_i, \quad (14)$$

where h , m , k , and R are Planck's constant, electron mass, Boltzmann constant, and Rydberg constant, respectively. The $n(p)$ distribution is thus determined by Eq. (14), using the parameters T_e and n_e derived in the previous section. Here, $n_i = n_e$ is assumed.

Stark broadening, Doppler broadening, and the instrumental function are taken into consideration for the line shapes. Stark broadening is evaluated for each observed line on the basis of theoretical data [12]. The instrumental function is measured with the 253.7-nm line from a mercury lamp and is approximated with a Gaussian function having FWHM = 0.090 nm. Doppler broadening due to atom temperature, which is assumed to be the same as T_e , is 0.067 nm (in FWHM), and the total Gaussian profile width is derived to be 0.11 nm (in FWHM). The whole line shape is obtained as a convolution with the Stark broaden-

ing profile.

The radiative recombination continuum is evaluated for the continuum radiation component in Fig. 5. The calculation method is described in detail in Ref. [13]. Its intensity relative to that of the line radiation, however, is found too low to explain the measured spectrum. The observed continuum radiation could be dominated by the bremsstrahlung in the bulk plasma, and we treat the continuum radiation component as a constant background signal in the present study.

Figure 5 shows the synthetic line radiation profiles along with the adjusted constant background. For the discrete lines, both the intensity distribution and the line shapes are consistent with the synthetic ones and the plasma parameters derived in the previous section are verified.

Acknowledgments

The authors are grateful to the LHD experimental group for their support. This study was partly supported by financial aid from the LHD project (NIFS07ULPP527).

- [1] J. Neuhauser, M. Alexander, G. Becker *et al.*, Plasma Phys. Control. Fusion **37**, A37 (1995).
- [2] C.S. Pitcher and P.C. Stangeby, Plasma Phys. Control. Fusion **39**, 779 (1997).
- [3] A. Loarte, R.D. Monk, J.R. Martín-Solís *et al.*, Nucl. Fusion **38**, 331 (1998).
- [4] N. Asakura, S. Sakurai, H. Tamai *et al.*, J. Nucl. Mater. **290-293**, 825 (2001).
- [5] U. Wenzel, K. McCormick, N. Ramasubramanian *et al.*, Nucl. Fusion **44**, 1130 (2004).
- [6] S. Masuzaki, R. Sakamoto, J. Miyazawa *et al.*, J. Plasma Fusion Res. **81**, 649 (2005).
- [7] J. Miyazawa, S. Masuzaki, R. Sakamoto *et al.*, Nucl. Fusion **46**, 532 (2006).
- [8] B.J. Peterson, A.Yu. Kostrioukov, N. Ashikawa *et al.*, Plasma Phys. Control. Fusion **45**, 1167 (2003).
- [9] T. Fujimoto, S. Miyachi and K. Sawada, Nucl. Fusion **28**, 1255 (1988).
- [10] M. Goto, K. Sawada and T. Fujimoto, Phys. Plasmas **9**, 4316 (2002).
- [11] NIST Atomic Spectra Database (<http://physics.nist.gov/PhysRefData/ASD/index.html>)
- [12] C. Stehlé and R. Hutcheon, Astron. Astrophys. Suppl. Ser. **140**, 93 (1999).
- [13] M. Goto, R. Sakamoto and S. Morita, Plasma Phys. Control. Fusion **49**, 1163 (2007).